Joule

CellPress
OPEN ACCESS

Article

Nanochannel electrodes facilitating interfacial transport for PEM water electrolysis

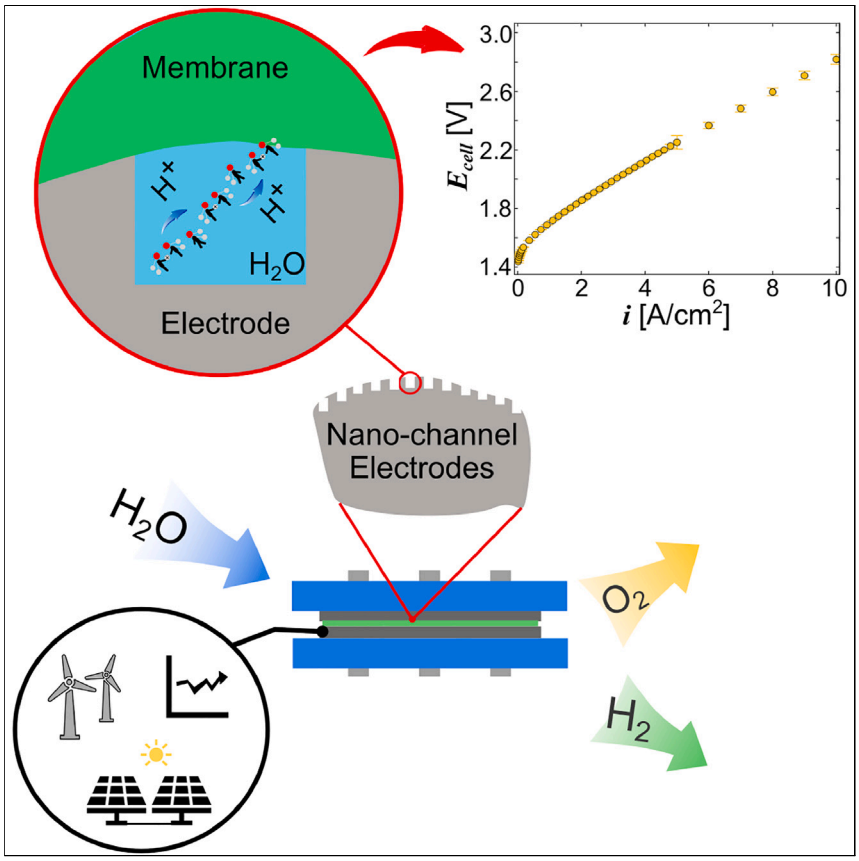

Addressing the convoluted interfacial transport phenomenon on the anode of proton-exchange membrane water electrolyzers remains a considerable challenge, which hinders further efficiency and durability improvement for the technology. Correspondingly, we couple electrochemical diagnostic techniques with characterization tools to unravel the potential proton hopping mechanism and imbalance of oxygen transport at the transport layer, catalyst layer, and membrane interfaces. The results guide us to design electrodes with nanochannels, which improve interfacial transport and achieve outstanding electrolysis performance and durability.

Jason K. Lee, Finn Babbe, Guanzhi Wang, Andrew W. Tricker, Rangachary Mukundan, Adam Z. Weber, Xiong Peng

xiongp@lbl.gov

Highlights

Possible proton hopping mechanism through water phase in PEMWE

Unravel the imbalance of oxygen production and removal under PTL islands

Electrodes with under-island nanochannels improve interfacial transport

Nanochannel electrodes achieve durable operation with reduced loadings

Lee et al., Joule 8, 2357–2373
August 21, 2024
Published by Elsevier Inc.
https://doi.org/10.1016/j.joule.2024.06.005

Joule

CellPress
OPEN ACCESS

Article

Nanochannel electrodes facilitating interfacial transport for PEM water electrolysis

Jason K. Lee,[1,2,3] Finn Babbe,[4] Guanzhi Wang,[1] Andrew W. Tricker,[1] Rangachary Mukundan,[1] Adam Z. Weber,[1] and Xiong Peng[1,5,*]

SUMMARY

Proton-exchange membrane water electrolyzers (PEMWEs) are a promising technology for green hydrogen production; however, interfacial transport behaviors are poorly understood, hindering device performance and longevity. Here, we first utilized finite-gap electrolyzer to demonstrate the possibility of proton transfer through water in PEMWEs. The measured high-frequency resistances (HFRs) exhibit a linear trend with increasing gap distance, where extrapolation shows a lower value compared with HFRs in regular zero-gap electrolyzers, indicating that ohmic resistance could be further reduced. We introduce nanochannels to facilitate mass transport, as evidenced by both liquid-fed and vapor-fed electrolysis. Nanochannel electrodes achieve a voltage reduction of 190 mV at 9 $A \cdot cm^{-2}$ compared with the Ir-PTEs without nanochannels. Furthermore, nanochannel electrodes show negligible degradation through 100,000 accelerated-stress tests and over 2,000 h of operation at 1.8 $A \cdot cm^{-2}$ with a decay rate of 11.66 $\mu V \cdot h^{-1}$. These results provide new insights into localized transport dynamics for PEMWEs and highlight the significance of interfacial engineering for electrochemical devices.

INTRODUCTION

Clean hydrogen, produced through water electrolysis coupling with renewable energy such as solar or wind,[1–3] has been an emerging means of curtailing undesired carbon footprints from hard-to-decarbonize sectors such as industrial[4–6] and heavy-duty transportation[7,8] sectors. Proton-exchange membrane (PEM) water electrolyzer (PEMWE) is a prominent water-splitting technology among other alternatives as it provides rapid response time suited for direct integration with intermittent renewable electricity and enables a compact stack design, simplifying the establishment of decentralized hydrogen production facilities.[9] However, stepping up from the current megawatt-scale PEMWE systems[10] to gigawatt (GW)-scale systems is a prerequisite to realize a widespread adoption of clean hydrogen technologies. Only 5% of hydrogen available in the global market today is produced from water electrolysis.[11] Reforming of hydrocarbons still remain as the mainstream method for hydrogen production due to their low cost, albeit they emit 9 kg of CO_2 for every kg of H_2 produced.[12] Recognizing the need, the U.S. Department of Energy has launched a Hydrogen Shot goal to achieve $1 per kg of clean hydrogen by 2030,[13] which targets to drive the production cost of clean hydrogen to be more competitive in the market.

A major barrier to the establishment of GW-scale electrolyzers is the use of excessive amount of platinum-group metals (PGMs) required for PEMWEs. Platinum is not only

CONTEXT & SCALE

Hydrogen, as a stable energy carrier, offers great potential to decarbonize hard-to-decarbonize sectors to combat climate change. Meeting the growing demand for low-carbon hydrogen hinges critically on the large-scale deployment of proton-exchange membrane (PEM) water electrolyzers to capture highly intermittent electrons from renewable resources. However, current commercial PEM water electrolyzers using excess platinum-group metal catalysts (such as iridium) present potential challenges to achieving this overarching goal. Despite substantial progress in developing novel catalysts materials, achieving highly efficient and durable PEM water electrolysis performance is still a grand challenge. Our solution is to rationally design electrodes with improved transport features to drastically improve efficiency and durability. This also allows us to reduce iridium usage by an order of magnitude compared with incumbent systems, which is critical to a sustainable hydrogen economy.

used as the cathode electrode,[14] but also as catalysts in the gas recombination layer,[15] and also as a protective coating layer on flow field and porous transport layers (PTLs).[16] Moreover, iridium (Ir), being the scarcest element on the Earth's crust, is used as the oxygen evolution reaction (OER: $2H_2O \rightarrow 4H^+ + O_2 + 4e^-$, $E^0 = 1.23$ V vs. SHE) catalyst on the anode, escalating the cost of PEMWEs.[17] The Ir loading used in commercial stacks ranges from 1.0 to 3.0 $mg_{Ir} \cdot cm^{-2}$,[18–20] however, the deployment of GW-scale PEMWEs would require reduction of Ir loading to approximately 0.05 $mg_{Ir} \cdot cm^{-2}$.[18] Perceiving the urgent need to reduce the anode Ir loading, research efforts have been made to design materials for PEMWEs at low Ir loadings (0.05~0.1 $mg_{Ir} \cdot cm^{-2}$) and to investigate critical factors impacting device performance and durability under these conditions.[21–24] Lewinski et al.,[24] have demonstrated a significant loading reduction with notable performance improvements by exploiting the benefits of a nanostructured thin film Ir electrode for PEMWEs. Moreover, supported Ir catalyst and confined Ir with single site have been developed to help further reduce catalyst loading by increasing electrochemical surface area (ECSA) and catalyst utilization of the anode electrodes.[25,26] Similarly, Hegg et al. fabricated an interlayer for low-loaded catalysts to enhance the electrical interconnectivity, which outperformed the conventional catalyst layer even with loadings exceeding 6-fold.[27] Other strategies, including designing porous electrodes[28,29] to facilitate mass transport and tuning reaction interfaces[30] by optimizing PTL structures, have been reported to effectively reduce Ir usage in PEMWEs. Although promising, translating material advancements into efficient and durable electrolyzers for industrial application still remains a significant hurdle.

One of the limitations of this translation comes from the use conventional electrodes, which are composed of catalyst nanoparticles mixed with ionomers, fabricated by coating an ink slurry to either the PEM or PTL to make catalyst-coated membrane (CCM) or porous transport electrode (PTE), respectively. Due to the complexity in controlling ink rheology, fabrication techniques, and condition, this process leaves little room for designing electrodes with expedited species transport, higher utilization of catalysts, and better interfacial compatibility with other components in membrane-electrode assembly (MEA) devices. Furthermore, a deficiency in comprehending the localized transport mechanism at the PTL/catalyst layer (CL)-PEM interfaces, where the co-existence of water, oxygen, protons, and electrons persists. Albeit the strong research interest in this interfacial behavior, there is still a lack of design guidance on how to fine-tune the interfacial structure to achieve superior device performance and longevity.

In this work, we first design experiments to elucidate the possibility of proton transport through water phase occurring on anode in PEMWEs and unravel the imbalance of oxygen gas transport between production by OER and removal at the PTL/CL-PEM interfaces. These investigations inspire us to design electrodes with nanochannels under the PTE islands that provide extra transport pathways to facilitate both oxygen diffusion and water transport, which avoids local oxygen buildup and therefore helps better hydrate the membrane and minimize interfacial contact resistance. Combining all these unique features, the nanochannel PTEs achieve excellent performance and durability from both accelerated-stress tests (ASTs) and constant current test at Ir loading of 0.12 $mg_{Ir} \cdot cm^{-2}$ for PEMWEs.

RESULTS

Experimental evidence of proton transfer through water phase in PEMWEs

Unveiling the mechanism of proton transfer is a prerequisite for understanding and designing optimized electrode structure for PEM water electrolyzers. The transport

[1]Energy Technology Area, Lawrence Berkeley National Laboratory, Berkeley, CA 94720, USA

[2]Department of Mechanical Engineering, University of Victoria, Victoria, BC V8P 5C2, Canada

[3]Institute for Integrated Energy Systems (IESVic), University of Victoria, Victoria, BC V8P 5C2, Canada

[4]Chemical Science Division, Lawrence Berkeley National Laboratory, Berkeley, CA 94720, USA

[5]Lead contact

*Correspondence: xiongp@lbl.gov

https://doi.org/10.1016/j.joule.2024.06.005

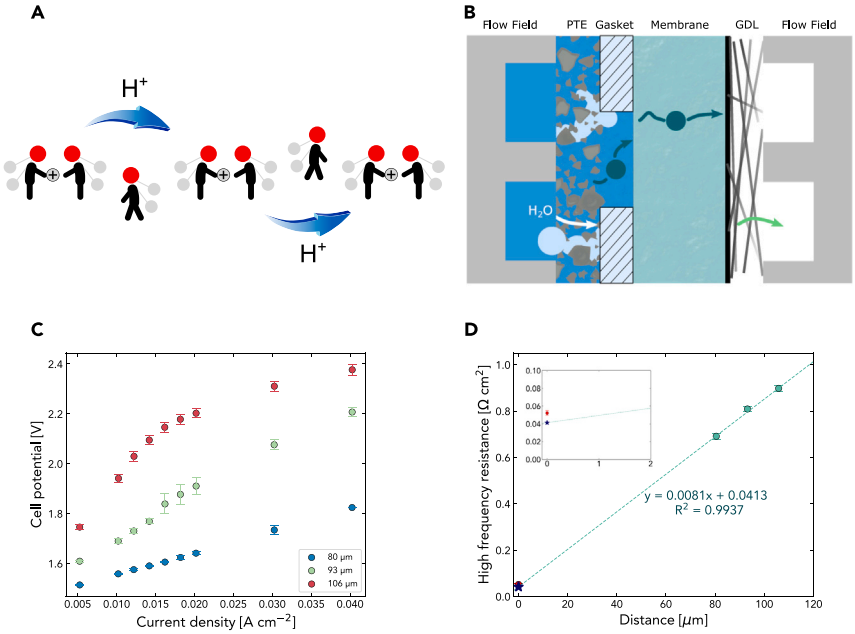

Figure 1. Investigation of proton transfer through liquid water in PEMWE

(A) Schematic describing the proton hopping mechanism, which would drive proton conduction through hydrogen bond network across different water molecules.

(B) Schematic of the finite-gap electrolyzer, where a finite gap is intentionally introduced using a gasket between the electrode and the proton-exchange membrane (drawings are not to scale).

(C) Polarization curves measured at various gap distances of 80, 93, and 106 μm, respectively. The performance deteriorates with increasing gap thickness.

(D) High-frequency resistances measured in a regular zero-gap PEM water electrolyzer (red data point) and at varying gap distances. The regression between HFR and gap distances shows a linear relation. The dark blue star marker indicates an ideal case where the gap distance is infinitely close to zero between the PTE and PEM. The inset shows the deviation in HFRs between the ideal case and the regular zero-gap water electrolyzer. The error bars represent the standard deviation of three independent measurements.

of protons in conventional ionomer electrodes is dominant and enhanced by the interaction with the sulfonic acid groups (–SO_3H) in the ionomer and the membrane, which involves multiple sequential processes of dissociation of the proton, formation of an ion-pair with water, and water-mediated transport through the hydrated domains.[31] Owing to the high concentration of –SO_3H and continuous network of ion-conducting channels, proton-conducting polymers often exhibit excellent proton conductivity. While ionomers play a key role in conducting protons from anode to the PEM in conventional electrode structure, the liquid water molecules on anode side offers an additional media for protons to transfer through the hydrogen bond network (Figure 1A) via the so-called proton hopping mechanism under the strong electric field between anode and PEM.[32,33]

To demonstrate this possible proton transfer mechanism in PEMWEs, electrochemical tests were performed in a finite-gap electrolyzer cell. As depicted in Figure 1B, a gasket was used to intentionally create a finite water-phase gap between the PTE and the PEM. By varying the thickness of the gasket, distance of the gap could be well controlled. The comparison of polarization curves between finite-gap and zero-gap water electrolyzers indicates at least two orders of magnitude difference in current density at ~1.8 V (Figure S1A), which rules out the possibility of PEM touching PTE in finite-gap measurements. The result indicates that even with the

presence of a finite gap between the PTE and PEM, protons can still migrate through the water phase, which enables water electrolysis operation (Figure 1C). The impurities of the water on anode were measured using inductively coupled plasma mass spectroscopy (ICP-MS), which was determined to contribute to negligible ionic conductivity (Table S1). As the gap distance increases, there is a significant drop in electrolysis performance (Figure 1C), which is mostly due to the increase in high-frequency resistance (HFR) (Figure 1D). In fact, we measured a linear relationship between the HFR and the gap distance, as shown in Figure 1D. The physical meaning of the y axis intercept of the linear relationship indicates a scenario where the PTE is infinitely close to the PEM; therefore, protons do not need to travel through the water phase (dark blue star in Figure 1D). It is worth noting that this scenario results in an HFR value of 0.0413 Ohms cm^2, which is approximately 26% lower than the measured HFR value in a regular zero-gap configuration (red data point in the inset of Figure 1D). As the membrane is likely to be fully hydrated by sufficient water in the presence of a gap, these results suggest that the membrane is not in a fully hydrated condition or that there exists extra ohmic resistance in a regular zero-gap configuration, which leads to higher HFR than the ideal scenario. To strengthen the observation of potential membrane dehydration in zero-gap water electrolyzers, we conducted a survey from the literature,[34–38] collecting proton conductivities of fully hydrated Nafion 212 membrane at 80°C, and computed the area-specific resistances as shown in Figure S1B and Table S2. The calculated area-specific resistances are indeed lower compared with the value we measured through HFR in a zero-gap electrolyzer cell.

Probe the PTL/CL-PEM interface

It is generally accepted that the anode CL that is in direct contact with PTL contributes to most of the anode reactions due to limited CL in-plane electric conductivity, especially at low Ir loadings.[39–41] Therefore, the post-operation anode CL exhibits two distinct morphologies, where the area that contacts the PTL shows indentation and deformation (Figure 2A), and the area that does not contact the PTL shows intact and flat surface (Figure 2B). When zooming into the indented region, there exists a group of irregular micro-sized cavities (Figure 2C), which are suspected to be formed due to the high oxygen pressure building up at the PTL/CL-PEM interfaces during electrolysis operation. Namely, the oxygen produced by OER could accumulate if the oxygen cannot be removed faster enough compared with the production rate, which could happen if the oxygen diffusion length is too long under the PTL island where the OER occurs (Figure 2D). It can be expected that the trapped oxygen can lead to enhanced local contact resistance and possible local membrane dehydration by impacting water supply. It is also discovered that the water supply to the PTL/CL-PEM interface is strongly impacted by high operational current densities, which exacerbates the local oxygen gas blockage issue.[43] These results suggest the imbalance between oxygen production and removal and the resultant impacts on device performance, as well as the need to redesign the PTL/CL-PEM interfaces to further tailor the localized water, oxygen gas, and proton transport.

Design of Ir-PTE with nanochannel features

Our approach to improving the localized species transport is to build extra pathways by creating nanochannels under the PTL islands, which are hypothesized to facilitate oxygen removal and water supply at the PTL/CL-PEM interfaces (Figure 3A). The under-island nanochannels (Figures 3B–3D) were fabricated using femtosecond laser ablation to the PTL surface. The ultrafast pulse width of the femtosecond laser restricts the surface modification of the PTL to be at nanoscale.[44] Specifically, these nanochannels are formed due to the interference of the incident laser with the excited surface plasmon polaritons, which results in spatial distribution of periodic

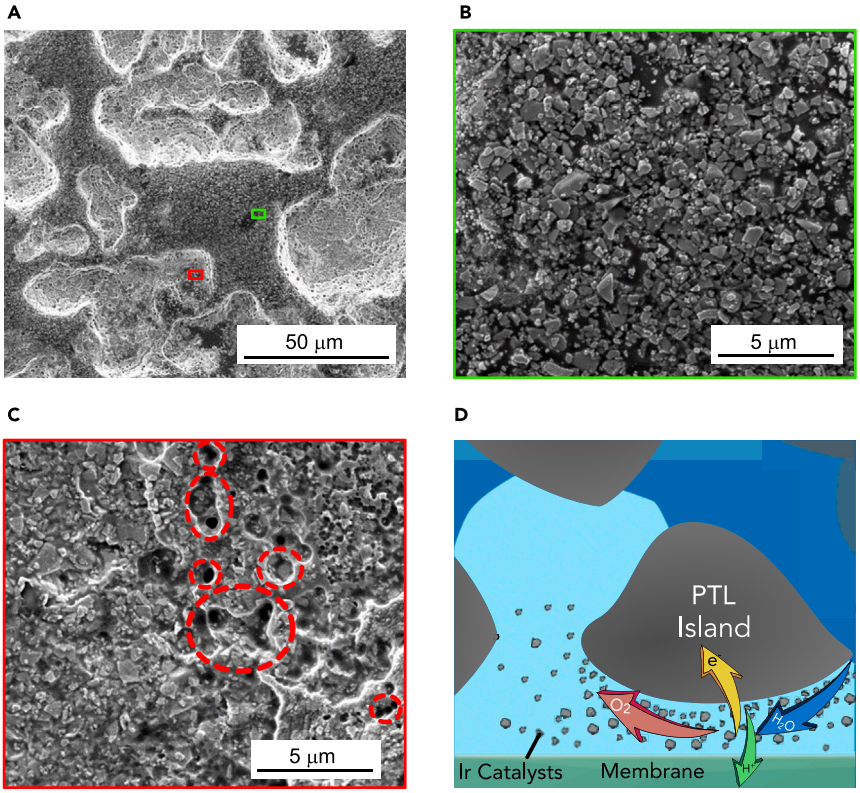

Figure 2. The transport dynamics at anode PTL/CL-PEM interface in PEMWE

(A) Scanning electron microscopy (SEM) image of post-operation anode CL showing two distinct morphologies with and without indentation. Anode catalyst layer was fabricated using a nanoporous Ir catalyst at loading of 0.05 $mg_{Ir} \cdot cm^2$.[42]

(B) Zoomed-in view of anode CL morphology revealing the flat domain (green rectangle in A) that is not in direct contact with the PTL island.

(C) Zoomed-in view of anode CL morphology revealing the indented domain (red rectangle in A) that is in direct contact with the PTL island. The circles highlight the micro-cavities induced by local oxygen trapping and pressure buildup, which potentially lead to higher local contact resistances and local dehydration of the membrane.

(D) A schematic describing the transport dynamics of reactant liquid water, oxygen gas, electrons, and protons at the anode PTL/CL-PEM interfaces.

energy on the surface.[45] The width of each nanochannel is measured to be in between 50 and 100 nm (Figure 3D), which allows the creation of densely packed nanochannels on each PTL island (Figure 3C). The femtosecond (FS) laser-ablated PTL was fabricated into PTE (denoted as FS Ir-PTE, Figure S2C) using physical vapor deposition (PVD) of Ir.[46] The PVD allows to create ionomer-free PTE with uniform Ir coating at low loadings (~0.1 $mg_{Ir} \cdot cm^2$). We also apply fiber laser ablation to create patterns at micrometer scale (Figure S2B), followed by femtosecond laser ablation to create nanochannels, which combined enable multi-scale laser patterns to Ir-PTE (denoted as MS Ir-PTE, Figure S2D). By applying fiber laser ablation to the PTL prior to femtosecond laser ablation, the interfacial area of the PTL could be further enhanced,[22] so more nanochannels could be inscribed. The depth of each nanochannel is measured to be ~100 nm via the cross-sectional view of the FS Ir-PTE imaged by focused-ion beam scanning electron microscopy (SEM) (Figure S3). PTL without any laser ablation was also fabricated into PTE (denoted as Ir-PTE; Figure S2A) as a control for the following studies. The surface composition and crystallographic structure of the Ir-PTE and MS Ir-PTE were analyzed using X-ray photoelectron spectroscopy

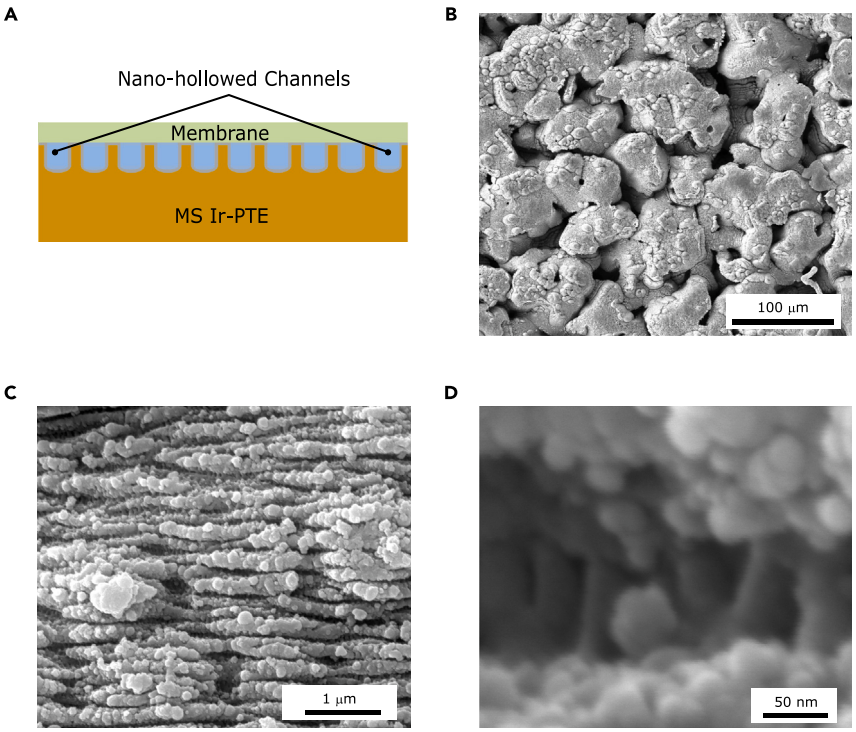

Figure 3. Surface structure of the nanochannel porous transport electrodes

(A) Schematic illustration of the PTE/PEM interfaces created by the nanochannel electrode.

(B) SEM image showing the surface of a multi-scale laser-ablated PTE (MS Ir-PTE).

(C) SEM image showing the surface morphology of nanochannel structure observed from a PTL island.

(D) Zoomed-in image of a single nanochannel structure.

(XPS) and X-ray diffraction (XRD), respectively. As indicated by the deconvoluted peaks from XPS, both Ir-PTE and MS Ir-PTE show identical surface Ir compositions with dominant metallic state and trace amount of IrOOH and IrO_2 (Figures S4A and S4B). The XRD patterns only show the diffraction peaks from the metallic Ir, which implies that the oxidized Ir is either amorphous or too thin to be detected by XRD (Figure S5). The contact angle measurements indicate that nanochannels improve water imbibition on electrode surface as water favors invading pores with high capillary pressure as wetting phase (Figure S6).

PEMWE performance of the nanochannel Ir-PTEs

As the depth of the nanochannels (Figure S3) is orders of magnitude lower than the typical thickness of membranes for PEMWEs, the thickness of the membrane is less likely to have direct impacts on performance of the FS and MS Ir-PTEs. We utilized Nafion 117 (dry thickness of 177.8 μm) for the rest of the PEMWE studies so that results can be directly compared with commercial systems.[20] Polarization curves were measured using Ir-PTE, FS Ir-PTE, and MS Ir-PTE in PEMWEs at anode and cathode loadings of 0.12 $mg_{Ir} \cdot cm^{-2}$ and 0.10 $mg_{Pt} \cdot cm^{-2}$, respectively (Figure 4A). The mass activity (MA) at 1.45 V and double-layer capacitance of each PTE were also measured to elucidate the impacts of nanochannels on the ECSA and catalyst utilization. Qualitatively speaking, the double-layer capacitance at the PTE/PEM interfaces could represent the electrode's ECSA for OER. As seen in Figure 4B, the increase in the measured double-layer capacitance is observed as nanochannels are inscribed at the PTE/PEM interface for both FS and MS Ir-PTEs. As the enlarged contact surface facilitated by the implementation of a fiber laser allocates

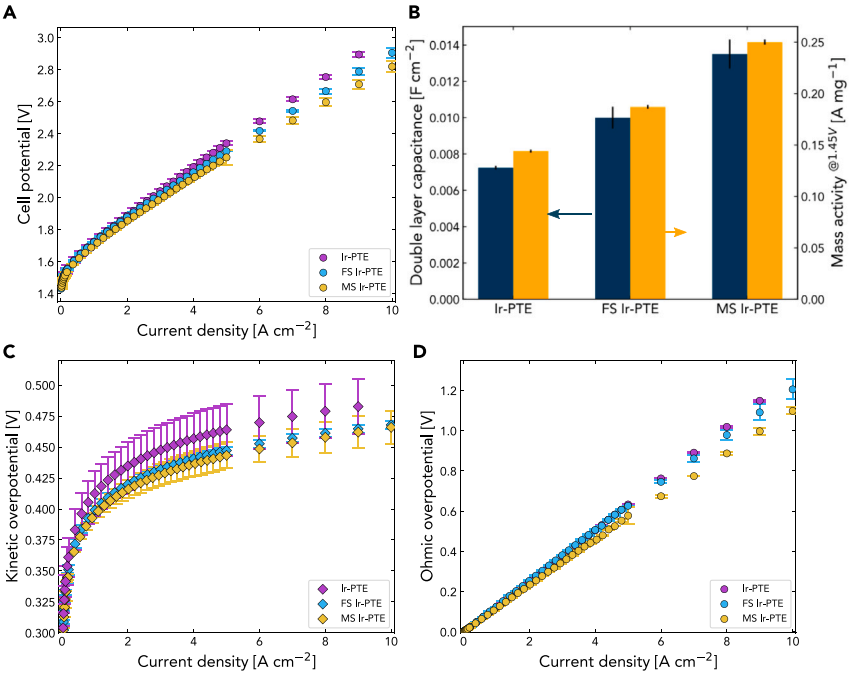

Figure 4. Electrochemical performance evaluation of Ir-PTE, FS Ir-PTE, and MS Ir-PTE

(A) PEMWE polarization curve comparison among three PTEs.

(B) Double-layer capacitance (dark blue) and mass activity at 1.45 V (yellow) measured for each electrode.

(C) Kinetic overpotential comparison among three PTEs.

(D) Ohmic overpotential comparison among three PTEs. The error bars represent the standard deviation of two independent measurements.

additional space for nanochannels to be carved onto, the MS Ir-PTE shows enhanced double-layer capacitance compared with FS Ir-PTE. The enhanced ECSA of nanochannel PTEs translates into improved catalyst utilization, as shown by the MA improvement (Figure 4B). Compared to Ir-PTE, the FS Ir-PTE and MS Ir-PTE achieve 30% and 74% of MA improvement, respectively, which correlates very well with the extent of double-layer capacitance enhancement. The lower kinetic overpotential for the FS Ir-PTE and MS Ir-PTE (Figure 4C) is also in line with the increased MA and increased double-layer capacitance, as well as the lower Tafel slopes measured from each experiment (Figure S7).

Without laser modification to create under-island nanochannels, PEMWE built with Ir-PTE exhibits reasonable performance, which achieves 2.19 V at 4 A·cm^{-2}, and 2.90 V at 9 A·cm^{-2} (the electrolyzer was not able to hold 10 A·cm^{-2} due to the prescribed safety limit of 3 V). PTEs with nanochannel features experience significantly lower cell potentials during polarization curve measurements, where the FS Ir-PTE cell demonstrates 2.16 V at 4 A·cm^{-2}, and 2.79 V at 9 A·cm^{-2} and the MS Ir-PTE cell achieves 2.13 V at 4 A·cm^{-2}, and 2.71 V at 9 A·cm^{-2}. Both the FS and MS Ir-PTEs, which are ionomer-free in the anode, can withstand a current density of 10 A·cm^{-2}, suggesting that proton conduction through water phase in nanochannels is not a limiting factor even at the high current densities. What benefits more to electrolysis performance by nanochannels is the reduction of ohmic loss (Figure 4D), suggesting better membrane hydration for FS and MS Ir-PTEs compared with Ir-PTE. Moreover, presence of nanochannels also help reduce residual overpotential loss (Figure S8), which is primarily related to mass transfer losses in PEMWEs,[47] even though the MS Ir-PTE experiences slightly higher residual loss

compared with FS Ir-PTE, probably due to that the fiber laser ablation creates larger PTL islands compared with pristine PTL (Figures S2A vs. S2B), leading to higher water and oxygen diffusion length under PTL islands. Nevertheless, these results suggest that the under-island nanochannels at the PTE/PEM interfaces could provide extra pathways to facilitate transport of water and oxygen gas, which, in turn, results in a reduction on the HFR and better electrode utilization.

Nanochannels facilitate localized interfacial transport

To further demonstrate the superiority of nanochannels under PTE island, providing extra pathways for water and oxygen transport and enhancing membrane hydration, we performed vapor-fed water electrolysis at various inlet relative humidities (RHs). As vapor-fed condition limits water supply,[48] the electrolyzer performance becomes more sensitive to water transport pathways. Therefore, vapor-fed electrolysis experiments can function as a touchstone to examine the efficacy of under-island nanochannels helping with water supply. Besides, the change of vapor RH offers an additional degree of freedom to probe how the water activity can impact PTE kinetics and reaction order. In general, as the decrease of vapor RHs, the electrolyzer shows deteriorated performance for both Ir-PTE and MS Ir-PTE (Figures 5A and 5B). However, nanochannels formed under the MS Ir-PTE islands help retain performance better. The PEMWE performance of MS Ir-PTE at RHs down to 70% remains identical to fully humidified condition (100% RH) and only starts to deviate at above 600 $mA \cdot cm^{-2}$. Even at lower RHs, the nanochannel MS Ir-PTE demonstrate superior performance that is comparable to the conventional catalyst layer used in the literature at much higher Ir loadings (1.0 vs. 0.12 $mg_{Ir} \cdot cm^{-2}$).[48] As the current increases, the vapor-fed electrolyzers exhibit mass transport-limited behavior due to limited water supply. It should also be noted that the MS Ir-PTE has overall higher mass transport-limited current densities, suggesting expedited mass transport compared with Ir-PTE. At a 100% RH, the electrolyzer achieves 1,600 $mA \cdot cm^{-2}$ near 2.4 V, which is approximately 2-fold increase compared with the Ir-PTE. The observed performance improvement can be attributed to the enhancement in water transport at the PTE/PEM interface facilitated by nanochannels under the MS Ir-PTE islands. This expedited species transport feature enabled by nanochannels not only provides reactant for anode OER but also helps better hydrate the membrane under low RHs conditions. As shown in Figure 5C, the MS Ir-PTE shows a lower uptrend of HFR increase as the decrease of RHs compared with that of the Ir-PTE, which further supports our hypothesis of enhanced transport characteristics by under-island nanochannels. The linear regression of reaction rate, i.e., the current density, against the reactant activity allows one to determine the OER reaction order at constant voltage. The OER reaction order of MS Ir-PTE is determined to be around 2.57, which is higher than the 2.1 of the conventional catalyst layers, probably due to reduced Ir loading by almost an order of magnitude.[49]

Nanochannels improve PEMWE durability

The impact of under-island nanochannels on durability of ionomer-free PTE was firstly evaluated using load-based AST protocols. Each PTE underwent a square wave current cycle consisting of 5 s hold at 0.4 $A \cdot cm^{-2}$ and 5 s hold at 3.2 $A \cdot cm^{-2}$ for a total of 100,000 cycles as a part of the AST protocol. The average current at each cycle is 1.8 $A \cdot cm^{-2}$, which matches operating current of commercial electrolyzer.[20,50] Polarization curves, electrochemical impedance spectroscopy (EIS), and cyclic voltammogram (CV) were measured after completion of every 10,000 cycle. The change in PEMWE performance over AST cycles for MS Ir-PTE and Ir-PTE is as shown in Figures 6A and 6B, respectively. Negligible degradation is observed for the MS Ir-PTE even after 100,000 cycles as the polarization curve at each AST stage largely overlaps with each other, especially at high currents (> 4 $A \cdot cm^{-2}$). In contrast, the Ir-PTE shows drastically higher degradation over the course of AST cycles,

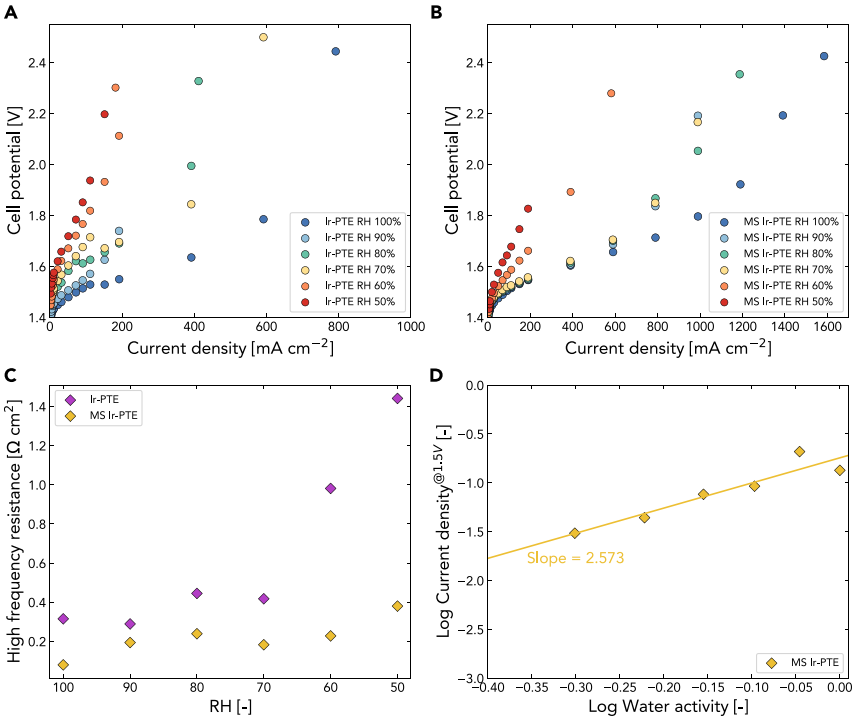

Figure 5. Electrochemical performance evaluation of the nanochannel electrode in vapor-fed electrolysis

(A) Polarization curves measured at various RHs during vapor-fed water electrolysis using Ir-PTE.

(B) Polarization curves measured at various RHs during vapor-fed water electrolysis using MS Ir-PTE.

(C and D) (C) High-frequency resistance comparison between the Ir-PTE and MS Ir-PTE at various inlet vapor RHs. Data were measured at 90 mA·cm^{-2} and (D) relation of logarithmic current density and logarithmic water activity/RH at constant voltage of 1.5 V using MS Ir-PTE during vapor-fed water electrolysis, the slope of the linear regression indicates the reaction order of water for oxygen evolution reaction.

leading to maximum difference of 214 mV after 100,000 AST cycles at 7 A·cm^{-2} (electrolyzer fails to hold 8 A·cm^{-2} after 100,000 cycles). The voltage profiles as a function of time during load-based AST cycling were recorded and shown in Figure 6C. Matching the excellent durability indicated by polarization curves at each AST stage, the two-end voltages corresponding to the two current densities for MS Ir-PTE did not show observable uptrend during the 100,000 AST cycling, while the two-end voltages of Ir-PTE experienced significant increase of 35 and 170 mV at 0.4 and 3.2 A·cm^{-2}, respectively. The postmortem SEM imaging of MS Ir-PTE surface (Figure S9) shows intact nanochannel features, while the energy-dispersive spectroscopy analysis shows lower Ir loss for the MS Ir-PTE compared with Ir-PTE, attributed to a better Ir retention on a roughened surface created by nanochannels. These results suggest the under-island nanochannels help improve PTE durability for PEM water electrolysis by protecting the PTE/PEM interfaces. It is also noteworthy that the voltage corresponding to 3.2 A·cm^{-2} decays over 4-fold compared with the voltage corresponding to 0.4 A·cm^{-2} for Ir-PTE during AST cycling (170 vs. 35 mV). This indicates AST protocols for MEA need to consider the electrolyzer performance loss at high currents to better evaluate comprehensive durability metrics.

The HFR for both PTEs remained relatively constant during AST cycling, indicating negligible change in PEM conductivity and interfacial contact resistance (Figure 6D); however,

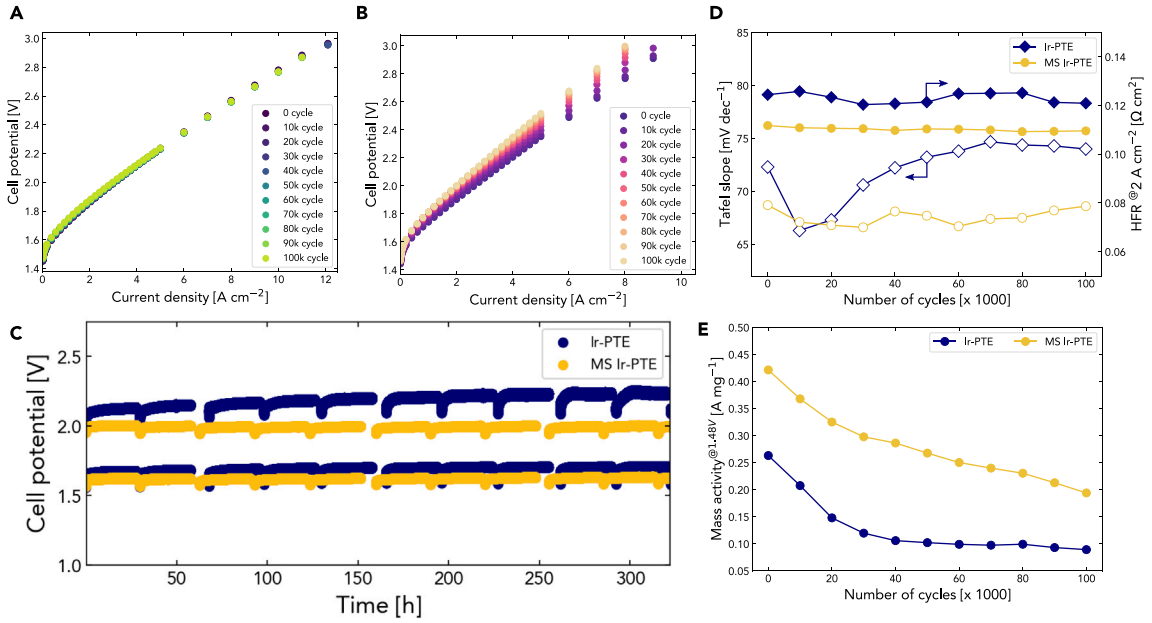

Figure 6. Impacts of nanochannel features on PEMWE durability evaluated using accelerated-stress tests

(A and B) Polarization curves measured every 10,000 cycles for total of 100,000 cycles of ASTs for (A) MS Ir-PTE and (B) Ir-PTE.

(C) Voltage profile comparison between MS Ir-PTE and Ir-PTE during 100,000 cycles of ASTs. The higher and lower voltages correspond to 3.2 and 0.4 $A \cdot cm^{-2}$ during AST, respectively.

(D) The measured Tafel slopes (hollow markers) and HFRs (solid markers) at various stages of AST cycles.

(E) Mass activity calculated using polarization curves at iR-free voltage of 1.48 V for both the MS Ir-PTE and Ir-PTE over 100,000 AST cycles.

the MS Ir-PTE showed a notably lower HFR compared with Ir-PTE during AST cycles. An interesting trend was observed in the measured Tafel slopes with the progression of AST cycles, where the Tafel slope decreased from the initial value of the pristine state for the first 20,000 cycles and kept increasing with further AST cycling, which was evident for both PTEs (Figure 6D). This is likely due to continued conditioning and electrode activation during the initial stage of AST cycling, while degradation starts to occur as prolonged AST cycling, mainly contributed by the decay of electrode activity. The Ir MA was recorded and compared between the MS Ir-PTE and Ir-PTE at each AST cycling stage. Note the MA was calculated using cell voltage of 1.48 V rather than 1.45 V due to the significant performance decay of Ir-PTE during the 100,000 AST cycles. At the beginning of life (BoL), the MA of the MS Ir-PTE is 59% higher than that of the Ir-PTE. This difference is attributed to the presence of nanochannels at the interface, which enhances ECSA and facilitates water and oxygen transport, as discussed in the previous section. Although both PTEs underwent MA loss over AST cycles, it should be noted that the MA of MS Ir-PTE could still be comparable to the MA of the BoL Ir-PTE even after 100,000 AST cycles. This enhancement in MA underscores the significance of the PTE/PEM interface created by under-island nanochannels in ionomer-free electrodes. It was also observed that the measured double-layer capacitances gradually increased with AST cycling for both PTEs (Figure S10), showing continued surface roughening of the PTE during AST. The XRD patterns of the PTEs at BoL and post-AST indicate similar crystallinity of the Ti phase of PTL, with slightly higher peaks observed for Ir (Figures S11 and S12). XPS measurements comparison between BoL and post-AST show that the surface Ir turns into oxides and oxyhydroxides from metallic state for both PTEs (Figure S13; Table S3), indicating that the Ir passivation contributes to the MA loss during AST. This change could suggest amorphous phase can form during ASTs, which corresponds to the increase of double-layer capacitance.

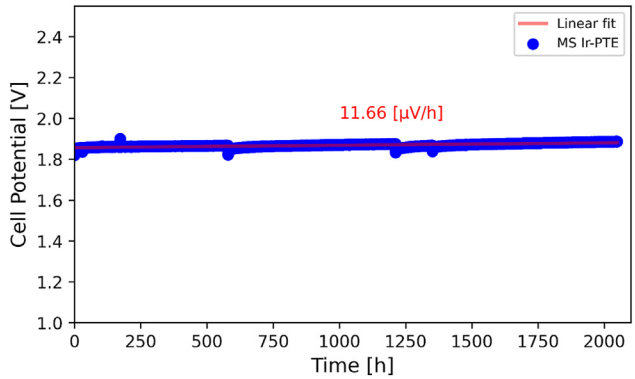

Figure 7. Long-term durability of PEMWE using nanochannel electrode

The MS Ir-PTE was operated at 1.8 $A \cdot cm^{-2}$ for 2,000 h at 80°C and ambient pressure. The spikes in between the long-term experiments refer to testing shutdowns and frequent replenishment of liquid water. The degradation rate observed from the stability test was 11.66 $\mu V \cdot h^{-1}$.

The durability of MS Ir-PTE was further examined using constant load test at current density of 1.8 $A \cdot cm^{-2}$ at 80°C and ambient pressure (Figure 7). The test was conducted for over 2,000 h, resulting in an average degradation rate of 11.66 $\mu V \cdot h^{-1}$, indicating exceptional durability of the MS Ir-PTE, especially given the low loading of 0.12 $mg_{Ir} \cdot cm^{-2}$ and 0.10 $mg_{Pt} \cdot cm^{-2}$ for anode and cathode, respectively. Notably, degradation occurs in a linear trend as it reaches a steady state. To put this into perspective, the MS Ir-PTE achieves lower degradation rate compared with the 36.5 $\mu V \cdot h^{-1}$ reported by Yu et al.[20] for a 2,500-h operation using low catalyst loadings at 50°C. It is also comparable to the degradation rate of 11.5 $\mu V \cdot h^{-1}$ observed in a commercial electrolyzer operating with catalyst loadings of 3 $mg_{Ir} \cdot cm^{-2}$ and 3 $mg_{Pt} \cdot cm^{-2}$ at 50°C.[20] In comparison to the durability of Ir-PTE at constant current (Figure S14), the MS Ir-PTE shows much lower decay rate (11.66 vs. 91.61 $\mu V \cdot h^{-1}$) despite tested at higher current (1.8 vs. 1.4 $A \cdot cm^{-2}$). These durability results further highlight the dual benefits of nanochannel electrodes, as they not only enhance performance but also elongate the lifespan of ionomer-free electrodes for PEMWEs.

DISCUSSION

The two critical aspects of Ir electrodes were elucidated in this work, encompassing the role of water in proton transport and the interfacial structure between PTE and PEM. We first used a finite-gap electrolyzer cell, which had a controlled distance between the PTE and the membrane, to reveal the possible proton transport through water phase by a possible hoping mechanism during PEM water electrolysis. The HFRs measured with increments of gap distance show a linear trend, which suggests that the ohmic resistance of PEMWE can be further reduced if under an ideal scenario, where the PEM is at fully hydrated condition. SEM images of post-operation anode catalyst layer shows that the PTL/CL-PEM interfaces can be deformed and dehydrated, which results from trapping oxygen gas due to a lack of efficient transport pathways at the interfaces. This inspired us to develop an advanced class of electrodes with nanochannel structures under the PTE island created by femtosecond laser ablation. These nanochannels are elucidated to facilitate water and oxygen gas transport at the PTE/PEM interfaces, therefore allowing better membrane hydration and reducing contact resistance. The nanochannel electrodes also have enhanced electrochemical active area and higher catalyst utilization. All these benefits created by nanochannels at the interface substantially improve PEMWE

performance compared with electrodes without nanochannels, reducing about 60 mV at 4 $A \cdot cm^{-2}$ and 190 mV at 9 $A \cdot cm^{-2}$. PTEs with nanochannels were also found to be more durable after even 100,000 of AST cycles. Under constant load operation of 1.8 $A \cdot cm^{-2}$, these electrodes showed exceptional durability up to 2,000 h with an average decay rate of just 11.66 $\mu V \cdot h^{-1}$. Overall, our work provides new insights on localized species transport mechanism that are highly valuable to the development of PTE and catalyst layer design and presents promising ionomer-free electrodes at low Ir loading for large-scale production of clean hydrogen.

EXPERIMENTAL PROCEDURES

Resource availability

Lead contact

Further information and requests for resources and materials should be directed to and will be fulfilled by the lead contact, Xiong Peng (xiongp@lbl.gov) upon request.

Materials availability

There are restrictions to the availability of nanochannel electrodes due to intellectual property ownership. However, authors will accommodate request under agreements.

Data and code availability

The data that support the findings of this study are included in the published article (and its supplemental information) or available from the lead contact upon request.

Nanochannel electrode fabrication

Fabrication of nanochannel electrodes includes processes of (1) femtosecond laser ablation and (2) Ir deposition. Femtosecond laser constructs nanochannel features at the PTL surface that contacts the membrane. To achieve this, a Coherent Libra system is used to generate laser pulses centered around 800 nm of wavelength with a pulse duration of 100 femtoseconds. An optical parametric amplifier (Coherent OpearA Solo) is subsequently used to generate pulses with a wavelength centered around 530 nm, which are used for the ablation. The beam is focused using a lens with a focal length of 500 mm to achieve a long depth of focus. The laser energy was adjusted using a graded neutral density filter to 20 μJ/pulse (~20 mW average power). The line spacing between ablation paths is kept at 20 μm.

To allocate more nanochannels at the PTL surface, fiber laser ablation was used to increase the PTL island area at the interface. For the fabrication of MS Ir-PTE, the PTL was ablated with a class 4 fiber laser (FIBER50FC, Full Spectrum Laser) before applying femtosecond laser ablation. The laser ablated the PTL in cross-hatching pattern with line spacing of 0.005 inch (127 μm), and a total of 100 passes were applied to enlarge the surface area. The laser featuring wavelength of 1,064 nm with spot size of 27 μm was applied at power of 10 W with pulse frequency of 80 kHz. Figure S15 describes the schematic of the fiber laser ablation process.

The PTLs were cleaned in a commercial etchant (Multi-etch) for 2 min and were rinsed with isopropanol and then with Milli-Q deionized water (18.2 $M\Omega \cdot cm$) for 2 min before Ir deposition. The ionomer-free PTEs were prepared by sputtering Ir directly onto (1) pristine sintered titanium powder-based PTLs (Mott) to fabricate Ir-PTEs,[46] (2) femtosecond laser-ablated PTLs to fabricate FS Ir-PTEs, and (3) both the fiber and femtosecond laser-ablated PTLs to fabricate MS Ir-PTEs. AJA Radio Frequency Sputtering System (AJA International) equipped with an Ir target (99.999%, Kurt J. Lesker) was used with a deposition rate of 1.75 $Å\ s^{-1}$ at 3 mTorr

under Argon atmosphere. The Ir loading of 0.12 $mg_{Ir} \cdot cm^{-2}$ was measured using X-ray fluorescence spectroscopy (Bruker M4 Tornado, Bruker). The loadings were accurately interpolated based on a calibration curve measured from six Ir and five Pt loadings of commercially available standards (Micromatter Technologies) along with a blank standard (0 $mg \cdot cm^{-2}$). The standard deviation of the measured loadings fell below 6%.

Fabrication of cathode CCMs

The cathode CCMs used as half-CCMs to pair with the PTEs were fabricated using ultrasonic spray coating. First, the Nafion 117 (Ion Power) membrane with a dry thickness of 177.8 μm was rested in Milli-Q DI water at boiling temperature for an hour and soaked in 0.5 M HNO_3 (ACS Reagent, Sigma-Aldrich) for another hour to remove any impurities in membranes and to protonate the sulfonic acid groups. The membranes were then rinsed three times before being stored in DI water until the catalyst deposition. The cathode ink was prepared by mixing platinum supported by carbon (TEC10V50E 46.8% Pt, Tanaka) with Milli-Q DI water and n-propanol at a ratio of 1:1 by volume and adding perfluorosulfonic acid (PFSA) ionomer solution (Nafion 5 wt %, Ion Power D521). The targeted ionomer-to-catalyst ratio was 0.45 for all half-CCMs fabricated in this work. The Sono-Tek ultrasonic spray coater was used for the deposition of the catalyst ink. The sonication rate at the nozzle was set to be 120 kHz, and the temperature of a vacuum table was set to be 80°C. Prior to the spraying, the cathode catalyst ink was dispersed through bath sonication for 30 min at 10°C. As soon as the bath sonication is completed, the cathode is sprayed until the targeted loading of 0.1 $mg_{Pt} \cdot cm^{-2}$ is attained.

Electrolyzer assembly and electrochemical performance testing

For all experiments conducted in this work, a single-cell hardware (Fuel Cell Technology [FCT]) was assembled with a platinum-coated single parallel channel anode titanium flow field and a single serpentine channel graphite cathode flow field. Due to the limit of maximum current for potentiostat, the active area of the electrolyzer was kept at 1 cm^2 as the testing current reached up to 10 $A \cdot cm^{-2}$. The fabricated ionomer-free Ir-PTEs were used as anode, and the fabricated half-CCM was used for the cathode. A commercially available carbon paper (Toray 120) coated with 5% polytetrafluoroethylene (PTFE) was used as the gas diffusion layer (GDL). The thickness of cathode ethylene tetrafluoroethylene (ETFE) gaskets was controlled to achieve 20% compression in the cathode GDL, whereas the thickness of anode ETFE gaskets matched the thickness of anode PTE. Eight bolts through the electrolyzer cell were torqued uniformly up to 4.5 Nm.

A Biologic VSP 300 potentiostat with a 20 A booster was used for all electrochemical analyses. A custom modified FCT test station was used for testing. A set of rod heater was used to control temperature of the electrolyzer cell at 80°C. Milli-Q deionized water was heated to 80°C and was used as anode reactant. The anode water was recirculated for the duration of the experiment. The cathode inlet was capped for the operation. Following protocols were used as a break-in process: (1) 30 CV measurements at a scan rate of 50 $mV \cdot s^{-1}$ between 1.2 and 2 V. (2) Two galvanostatic polarization curves measured by holding at various currents from open circular voltage (OCV) to 4 $A \cdot cm^{-2}$ with 1-min holds. Once the break-in procedure has been completed, another set of polarization curves was measured followed by measurement of galvanostatic EIS at each current step with frequency between 1 MHz and 100 mHz. The amplitude of the current was optimized for each step to ensure a sufficient signal-to-noise ratio while maintaining a linear system response. The maximum threshold voltage was set to 3.00 V. Lastly, 5 CV cycles were measured

each at a scan rate of 25, 50, 75, 100, and 125 $mV \cdot s^{-1}$ between 0.05 and 1.2 V, respectively.

Vapor-fed electrolyzer performance testing

Vapor-fed electrolysis testing was conducted with inlet feed of humidified N_2 (200 sccm) at various RH conditions of 50%, 60%, 70%, 80%, 90%, and 100%. The experiment started at 100% RH in decrements of 10%. Prior to each vapor-fed experiment, the cell was purged for at least 60 min at the tested RH condition with N_2 to ensure that there was no liquid water present in the electrolyzer cell. Electrochemical measurements including polarization curves and EIS were performed identical to water-fed electrolyzers.

Finite-gap electrolyzer testing

Finite-gap cell studies were conducted by positioning additional gaskets between the Ir-PTE and the PEM, as shown in Figure S16. The anode was prepared identically as described above, except Ir-PTE with geometric area of 5 cm^2 was used and masked down to active area of 1 cm^2, using the gasket for the gap. To minimize the impacts of membrane thermal expansion on gap distance, Nafion 212 membrane (dry thickness 50.8 μm) was used in the gap studies instead of Nafion 117. The gap distance is controlled by changing the thickness of this gasket. To minimize the membrane swelling effects on actual gap distance, the PEM is soaked in water for more than 48 h to ensure full hydration before cell assembly. Electrochemical measurements including polarization curves and EIS were performed. When calculating the actual gap thickness, both the thermal expansion of PEM ($\delta_{membrane\ thermal\ expansion}$) and the deformation of PEM by clamping pressure were considered. From fully hydrated condition at room temperature (23°C) to 80°C under MEA condition, the linear thermal expansion is about 5% at maximum for Nafion 212.[51] The average GDL thickness on cathode after operation was measured to be around 298 μm by a caliper. Given the thickness of gasket used on cathode was 254 μm, the compression by clamping pressure could lead to the PEM deformation by 298–254 μm = 44 μm. Therefore, the estimated distance of gap (d_{actual}) was calculated by the following equation:

$$d_{actual} = d_{gasket\ for\ gap} - \left(d_{GDL\ after\ compression} - d_{gasket\ for\ cathode}\right) - \delta_{membrane\ thermal\ expansion} = d_{gasket\ for\ gap} - (298\ \mu m - 254\ \mu m) - 5\% \cdot 50.8\ \mu m$$

Where $d_{gasket\ for\ gap}$ stands for the thickness used for the gap, which were 127, 139.7, and 152.4 μm for three conditions.

AST protocols

Galvanostatic-based AST protocols were implemented to assess the durability of Ir-PTE and MS Ir-PTE. A square waved current cycle of 5 s holds at two different currents (i_{Low} = 0.40 and i_{High} = 3.2 $A \cdot cm^{-2}$) was applied to the electrolyzer cell for a total 100,000 cycles. The catalyst loadings of the PTEs were at 0.12 $mg_{Ir} \cdot cm^{-2}$. Polarization curves, EIS, and CV were measured after completion of each 10,000 cycle to monitor degradation processes. The Ir MA was calculated by using current density at iR-free voltage of 1.45 or 1.48 V.

SEM and focused-ion beam SEM

The surface morphology of nanochannel electrodes was characterized using SEM (FEI Quanta FEG 250). Freshly fabricated samples were placed into the specimen chamber under high vacuum (<2×10^{-5} Torr). The energy level of the beam varied between 5 and 30 kV. Cross-sectional images of the nanochannel electrodes were acquired using an FEI Helios G4 dual-beam focused-ion beam (FIB) system with a Ga^+ ion beam. The cross section was cut out using the Ga^+ ion beam, and the section

was imaged using the electron beam. Through-the-lens detector under immersion mode at 5.0 kV and 0.1 nA with working distance set at 4 mm was used for imaging.

XRD

The chemical composition and crystallographic structure of the Ir present at the PTE were analyzed using a Rigaku Smartlab X-ray diffractometer equipped with a HyPix-3000 high-energy resolution 2D detector. Measurements are performed in Bragg-Brentano geometry with slow scan speeds of 2°/min.

XPS

The surface composition of Ir present at the PTE was determined via X-ray photoemission spectroscopy performed with a Kratos Axis Ultra DLD system. Measurements are carried out under ultrahigh vacuum (7.5×10^{-9} Torr) using a monochromatic Al Kα source for excitation. High-resolution spectra are acquired for the energy ranges around the Ir 4f, C 1s, and O 1s emission lines. Spectral energy positions are verified using adventitious C 1s and are within 0.3 eV of the expected 284.8 eV. Data analysis and fitting are done using CasaXPS software.

ICP-MS

Determination of residual ions in the water solutions was performed by ICP-MS (ICP-MS 7900, Agilent). Samples were acidified with ultrapure concentrated nitric acid before injection. A calibration curve ranging from 1 to 1,000 ppb made of a multi-element standard was used for quantification, and multiple internal standards (Sc, Ge) were used to correct for instrumentation drift and matrix effects.

Contact angle measurement

The contact angles of the Ir-PTE, FS-PTE, and MS-PTE were measured with a goniometer setup. A stage was set to hold a single PTE in place, aligned to the camera. A light source was used to ensure sufficient lighting for the camera. Only fully dried PTEs were used to the measurement. A droplet of DI water was placed onto the PTE for the measurement. 10 instances of contact angle were measured, and the average value was used.

SUPPLEMENTAL INFORMATION

Supplemental information can be found online at https://doi.org/10.1016/j.joule.2024.06.005.

ACKNOWLEDGMENTS

The authors sincerely acknowledge the Department of Energy-Office of Energy Efficiency and Renewable Energy-Hydrogen and Fuel Cell Technologies Office (DOE-EERE-HFTO) and the H_2 from the Next-generation of Electrolyzers of Water (H2NEW) consortium for funding under contract number DE-AC02-05CH11231. Work at the Molecular Foundry was supported by the Office of Science, Office of Basic Energy Sciences, of the U.S. Department of Energy under contract no. DE-AC02-05CH11231. All opinions expressed in this paper are the author's and do not necessarily reflect the policies and views of DOE.

AUTHOR CONTRIBUTIONS

J.K.L. performed most of the electrode fabrication, cell testing, characterization, and data analysis. F.B. performed femtosecond laser ablation, XPS, and ICP-MS. G.W. performed XPS data analysis. A.W.T. performed part of the cell testing. X.P. and A.Z.W. conceived the project. All authors contributed to writing. J.K.L. and X.P.

were the primary authors of the paper and chiefly responsible for the experimental design and data analysis.

DECLARATION OF INTERESTS

X.P. and A.Z.W. report on financial support provided by the Hydrogen and Fuel Cell Technologies Office. J.K.L., A.Z.W., and X.P. have patent Treatment of A Porous Transport Layer for Use in An Electrolyzer pending to The Regents of The University of California.

Received: January 29, 2024
Revised: April 1, 2024
Accepted: June 4, 2024
Published: June 25, 2024

REFERENCES

1. Wikramanayake, E., Acharya, P.V., Kapner, M., and Bahadur, V. (2021). Green hydrogen-based energy storage in Texas for decarbonization of the electric grid. In IEEE Green Technologies Conference, *1234*, pp. 409–415. https://doi.org/10.1109/GreenTech48523.2021.00070.

2. Alia, S.M., Stariha, S., and Borup, R.L. (2019). Electrolyzer durability at low catalyst loading and with dynamic operation. J. Electrochem. Soc. *166*, F1164–F1172. https://doi.org/10.1149/2.0231915jes.

3. Carmo, M., Fritz, D.L., Mergel, J., and Stolten, D. (2013). A comprehensive review on PEM water electrolysis. Int. J. Hydrog. Energy *38*, 4901–4934. https://doi.org/10.1016/j.ijhydene.2013.01.151.

4. Zhang, H., Wang, L., Van Herle, J., Maréchal, F., and Desideri, U. (2020). Techno-economic comparison of green ammonia production processes. Appl. Energy *259*, 114135. https://doi.org/10.1016/J.APENERGY.2019.114135.

5. Nayak-Luke, R., Bañares-Alcántara, R., and Wilkinson, I. (2018). "Green" ammonia: impact of renewable energy intermittency on plant sizing and levelized cost of ammonia. Ind. Eng. Chem. Res. *57*, 14607–14616. https://doi.org/10.1021/ACS.IECR.8B02447.

6. Rechberger, K., Spanlang, A., Sasiain Conde, A., Wolfmeir, H., and Harris, C. (2020). Green hydrogen-based direct reduction for low-carbon steelmaking. Steel Res. Int. *91*, 2000110. https://doi.org/10.1002/SRIN.202000110.

7. Lee, C., Kort-Kamp, W.J.M., Yu, H., Cullen, D.A., Patterson, B.M., Arman, T.A., Komini Babu, S., Mukundan, R., Borup, R.L., and Spendelow, J.S. (2023). Grooved electrodes for high-power-density fuel cells. Nat. Energy *8*, 685–694. https://doi.org/10.1038/s41560-023-01263-2.

8. Cullen, D.A., Neyerlin, K.C., Ahluwalia, R.K., Mukundan, R., More, K.L., Borup, R.L., Weber, A.Z., Myers, D.J., and Kusoglu, A. (2021). New roads and challenges for fuel cells in heavy-duty transportation. Nat. Energy *6*, 462–474. https://doi.org/10.1038/s41560-021-00775-z.

9. Millet, P., Mbemba, N., Grigoriev, S.A., Fateev, V.N., Aukauloo, A., and Etiévant, C. (2011). Electrochemical performances of PEM water electrolysis cells and perspectives. Int. J. Hydrog. Energy *36*, 4134–4142. https://doi.org/10.1016/j.ijhydene.2010.06.105.

10. Grigoriev, S.A., Fateev, V.N., Bessarabov, D.G., and Millet, P. (2020). Current status, research trends, and challenges in water electrolysis science and technology. Int. J. Hydrog. Energy *45*, 26036–26058. https://doi.org/10.1016/j.ijhydene.2020.03.109.

11. Bianco, E., and Blanco, H. (2020). Green Hydrogen: a Guide to Policy Making (Interrnational Renewable Energy Agency).

12. Ali Khan, M.H., Daiyan, R., Neal, P., Haque, N., MacGill, I., and Amal, R. (2021). A framework for assessing economics of blue hydrogen production from steam methane reforming using carbon capture storage & utilisation. Int. J. Hydrog. Energy *46*, 22685–22706. https://doi.org/10.1016/J.IJHYDENE.2021.04.104.

13. US Department of Energy (2023). U.S. National Clean Hydrogen Strategy and Roadmap. https://www.hydrogen.energy.gov/library/roadmaps-vision/clean-hydrogen-strategy-roadmap.

14. Kang, Z., Yang, G., Mo, J., Li, Y., Yu, S., Cullen, D.A., Retterer, S.T., Toops, T.J., Bender, G., Pivovar, B.S., et al. (2018). Novel thin/tunable gas diffusion electrodes with ultra-low catalyst loading for hydrogen evolution reactions in proton exchange membrane electrolyzer cells. Nano Energy *47*, 434–441. https://doi.org/10.1016/J.NANOEN.2018.03.015.

15. Ayers, K., Danilovic, N., Ouimet, R., Carmo, M., Pivovar, B., and Bornstein, M. (2019). Perspectives on low-temperature electrolysis and potential for renewable hydrogen at scale. Annu. Rev. Chem. Biomol. Eng. *10*, 219–239. https://doi.org/10.1146/ANNUREV-CHEMBIOENG-060718-030241.

16. Liu, C., Wippermann, K., Rasinski, M., Suo, Y., Shviro, M., Carmo, M., and Lehnert, W. (2021). Constructing a multifunctional interface between membrane and porous transport layer for water electrolyzers. ACS Appl. Mater. Interfaces *13*, 16182–16196. https://doi.org/10.1021/acsami.0c20690.

17. Minke, C., Suermann, M., Bensmann, B., and Hanke-Rauschenbach, R. (2021). Is iridium demand a potential bottleneck in the realization of large-scale PEM water electrolysis? Int. J. Hydrog. Energy *46*, 23581–23590. https://doi.org/10.1016/j.ijhydene.2021.04.174.

18. Bernt, M., Hartig-Weiß, A., Tovini, M.F., El-Sayed, H.A., Schramm, C., Schröter, J., Gebauer, C., and Gasteiger, H.A. (2020). Current challenges in catalyst development for PEM water electrolyzers. Chem. Ing. Tech. *92*, 31–39. https://doi.org/10.1002/CITE.201900101.

19. Ayers, K.E., Renner, J.N., Danilovic, N., Wang, J.X., Zhang, Y., Maric, R., and Yu, H. (2016). Pathways to ultra-low platinum group metal catalyst loading in proton exchange membrane electrolyzers. Catal. Today *262*, 121–132. https://doi.org/10.1016/J.CATTOD.2015.10.019.

20. Yu, H., Danilovic, N., Wang, Y., Willis, W., Poozhikunnath, A., Bonville, L., Capuano, C., Ayers, K., and Maric, R. (2018). Nano-size IrOx catalyst of high activity and stability in PEM water electrolyzer with ultra-low iridium loading. Appl. Catal. B *239*, 133–146. https://doi.org/10.1016/J.APCATB.2018.07.064.

21. Taie, Z., Peng, X., Kulkarni, D., Zenyuk, I.V., Weber, A.Z., Hagen, C., and Danilovic, N. (2020). Pathway to complete energy sector decarbonization with available iridium resources using ultralow loaded water electrolyzers. ACS Appl. Mater. Interfaces *12*, 52701–52712. https://doi.org/10.1021/acsami.0c15687.

22. Lee, J.K., Schuler, T., Bender, G., Sabharwal, M., Peng, X., Weber, A.Z., and Danilovic, N. (2023). Interfacial engineering via laser ablation for high-performing PEM water electrolysis. Appl. Energy *336*, 120853. https://doi.org/10.1016/j.apenergy.2023.120853.

23. Peng, X., Satjaritanun, P., Taie, Z., Wiles, L., Keane, A., Capuano, C., Zenyuk, I.V., and Danilovic, N. (2021). Insights into interfacial and bulk transport phenomena affecting proton exchange membrane water electrolyzer performance at ultra-low iridium loadings. Adv. Sci. *8*, e2102950. https://doi.org/10.1002/ADVS.202102950.

24. Lewinski, K.A., van der Vliet, D., and Luopa, S.M. (2015). NSTF advances for PEM electrolysis – the effect of alloying on activity of NSTF electrolyzer catalysts and performance of

NSTF based PEM electrolyzers. ECS Meeting Abstracts MA2015-02 *1234*, 1457. https://doi.org/10.1149/MA2015-02/37/1457.

25. Shi, Z., Wang, Y., Li, J., Wang, X., Wang, Y., Li, Y., Xu, W., Jiang, Z., Liu, C., Xing, W., et al. (2021). Confined Ir single sites with triggered lattice oxygen redox: toward boosted and sustained water oxidation catalysis. Joule *5*, 2164–2176. https://doi.org/10.1016/J.JOULE.2021.05.018.

26. Van Pham, C.V., Bühler, M., Knöppel, J., Bierling, M., Seeberger, D., Escalera-López, D., Mayrhofer, K.J.J., Cherevko, S., and Thiele, S. (2020). IrO_2 coated TiO_2 core-shell microparticles advance performance of low loading proton exchange membrane water electrolyzers. Appl. Catal. B *269*, 118762. https://doi.org/10.1016/J.APCATB.2020.118762.

27. Hegge, F., Lombeck, F., Cruz Ortiz, E., Bohn, L., von Holst, M., Kroschel, M., Hübner, J., Breitwieser, M., Strasser, P., and Vierrath, S. (2020). Efficient and stable low iridium loaded anodes for PEM water electrolysis made possible by nanofiber interlayers. ACS Appl. Energy Mater. *3*, 8276–8284. https://doi.org/10.1021/acsaem.0c00735.

28. Xie, Z., Ding, L., Yu, S., Wang, W., Capuano, C.B., Keane, A., Ayers, K., Cullen, D.A., Meyer, H.M., and Zhang, F.-Y. (2024). Ionomer-free nanoporous iridium nanosheet electrodes with boosted performance and catalyst utilization for high-efficiency water electrolyzers. Appl. Catal. B *341*, 123298. https://doi.org/10.1016/j.apcatb.2023.123298.

29. Ding, L., Wang, W., Xie, Z., Li, K., Yu, S., Capuano, C.B., Keane, A., Ayers, K., and Zhang, F.-Y. (2023). Highly porous iridium thin electrodes with low loading and improved reaction kinetics for hydrogen generation in PEM electrolyzer cells. ACS Appl. Mater. Interfaces *15*, 24284–24295. https://doi.org/10.1021/acsami.2c23304.

30. Yu, S., Li, K., Wang, W., Xie, Z., Ding, L., Kang, Z., Wrubel, J., Ma, Z., Bender, G., Yu, H., et al. (2022). Tuning catalyst activation and utilization via controlled electrode patterning for low-loading and high-efficiency water electrolyzers. Small *18*, e2107745. https://doi.org/10.1002/smll.202107745.

31. Kusoglu, A., and Weber, A.Z. (2017). New insights into perfluorinated sulfonic-acid ionomers. Chem. Rev. *117*, 987–1104. https://doi.org/10.1021/acs.chemrev.6b00159.

32. Popov, I., Zhu, Z., Young-Gonzales, A.R., Sacci, R.L., Mamontov, E., Gainaru, C., Paddison, S.J., and Sokolov, A.P. (2023). Search for a Grotthuss mechanism through the observation of proton transfer. Commun. Chem. *6*, 77. https://doi.org/10.1038/s42004-023-00878-6.

33. Hassanali, A., Giberti, F., Cuny, J., Kühne, T.D., and Parrinello, M. (2013). Proton transfer through the water gossamer. Proc. Natl. Acad. Sci. USA *110*, 13723–13728. https://doi.org/10.1073/pnas.1306642110.

34. Barique, M.A., Tsuchida, E., Ohira, A., and Tashiro, K. (2018). Effect of elevated temperatures on the states of water and their correlation with the proton conductivity of nafion. ACS Omega *3*, 349–360. https://doi.org/10.1021/acsomega.7b01765.

35. Lin, C.-C., Lien, W.-F., Wang, Y.-Z., Shiu, H.-W., and Lee, C.-H. (2012). Preparation and performance of sulfonated polyimide/nafion multilayer membrane for proton exchange membrane fuel cell. J. Power Sources *200*, 1–7. https://doi.org/10.1016/j.jpowsour.2011.10.001.

36. Thuc, V.D., Cong Tinh, V.D., and Kim, D. (2022). Simultaneous improvement of proton conductivity and chemical stability of Nafion membranes via embedment of surface-modified ceria nanoparticles in membrane surface. J. Membr. Sci. *642*, 119990. https://doi.org/10.1016/j.memsci.2021.119990.

37. Lufrano, E., Simari, C., Di Vona, M.L., Nicotera, I., and Narducci, R. (2021). How the morphology of nafion-based membranes affects proton transport. Polymers *13*, 359. https://doi.org/10.3390/polym13030359.

38. Yang, X., Kim, J.H., and Kim, Y.J. (2022). Enhanced proton conductivity of poly(ether sulfone) multi-block copolymers grafted with densely pendant sulfoalkoxyl side chains for proton exchange membranes. Polymer *242*, 124604. https://doi.org/10.1016/j.polymer.2022.124604.

39. Yang, G., Yu, S., Kang, Z., Li, Y., Bender, G., Pivovar, B.S., Green, J.B., Cullen, D.A., and Zhang, F.Y. (2020). Building electron/proton nanohighways for full utilization of water splitting catalysts. Adv. Energy Mater. *10*, 1903871. https://doi.org/10.1002/aenm.201903871.

40. Schuler, T., Schmidt, T.J., and Büchi, F.N. (2019). Polymer electrolyte water electrolysis: correlating performance and porous transport layer structure: Part II. Electrochemical performance analysis. J. Electrochem. Soc. *166*, F555–F565. https://doi.org/10.1149/2.1241908jes.

41. Schuler, T., De Bruycker, R., Schmidt, T.J., and Büchi, F.N. (2019). Polymer electrolyte water electrolysis: correlating porous transport layer structural properties and performance: Part I. Tomographic analysis of morphology and topology. J. Electrochem. Soc. *166*, F270–F281. https://doi.org/10.1149/2.0561904jes.

42. Chatterjee, S., Peng, X., Intikhab, S., Zeng, G., Kariuki, N.N., Myers, D.J., Danilovic, N., and Snyder, J. (2021). Nanoporous iridium nanosheets for polymer electrolyte membrane electrolysis. Adv. Energy Mater. *11*, 2101438. https://doi.org/10.1002/aenm.202101438.

43. Wang, W., Ding, L., Xie, Z., Yu, S., Canfield, B., Bender, G., Wrubel, J.A., Pivovar, B.S., and Zhang, F.-Y. (2023). Discovering reactant supply pathways at electrode/PEM reaction interfaces via a tailored interface-visible characterization cell. Small *19*, e2207809. https://doi.org/10.1002/smll.202207809.

44. Rukosuyev, M.V., Lee, J., Cho, S.J., Lim, G., and Jun, M.B.G. (2014). One-step fabrication of superhydrophobic hierarchical structures by femtosecond laser ablation. Appl. Surf. Sci. *313*, 411–417. https://doi.org/10.1016/J.APSUSC.2014.05.224.

45. Vorobyev, A.Y., and Guo, C. (2013). Direct femtosecond laser surface nano/microstructuring and its applications. Laser Photon. Rev. *7*, 385–407. https://doi.org/10.1002/lpor.201200017.

46. Lee, J.K., Anderson, G., Tricker, A.W., Babbe, F., Madan, A., Cullen, D.A., Arregui-Mena, J.D., Danilovic, N., Mukundan, R., Weber, A.Z., et al. (2023). Ionomer-free and recyclable porous-transport electrode for high-performing proton-exchange-membrane water electrolysis. Nat. Commun. *14*, 4592. https://doi.org/10.1038/s41467-023-40375-x.

47. Babic, U., Schmidt, T.J., and Gubler, L. (2018). Communication — contribution of catalyst layer proton transport resistance to voltage loss in polymer electrolyte water electrolyzers. J. Electrochem. Soc. *165*, J3016–J3018. https://doi.org/10.1149/2.0031815jes.

48. Fornaciari, J.C., Gerhardt, M.R., Zhou, J., Regmi, Y.N., Danilovic, N., Bell, A.T., and Weber, A.Z. (2020). The role of water in vapor-fed proton-exchange-membrane electrolysis. J. Electrochem. Soc. *167*, 104508. https://doi.org/10.1149/1945-7111/AB9B09.

49. Schuler, T., Kimura, T., Schmidt, T.J., and Büchi, F.N. (2020). Towards a generic understanding of oxygen evolution reaction kinetics in polymer electrolyte water electrolysis. Energy Environ. Sci. *13*, 2153–2166. https://doi.org/10.1039/D0EE00673D.

50. Yu, H., Bonville, L., Jankovic, J., and Maric, R. (2020). Microscopic insights on the degradation of a PEM water electrolyzer with ultra-low catalyst loading. Appl. Catal. B *260*, 118194. https://doi.org/10.1016/J.APCATB.2019.118194.

51. Nafion Membrane Chart. https://www.fuelcellearth.com/nafion-membrane-chart/.